Applied Surface Science 487 (2019) 1096–1103

Contents lists available at ScienceDirect

Applied Surface Science

journal homepage: www.elsevier.com/locate/apsusc

Full length article

# Enhancement in bio-corrosion resistance of metallic glass by severe surface deformation

Gopinath Perumal[a], Harpreet Singh Grewal[a], Aditya Ayyagari[b,c], Sundeep Mukherjee[b], Harpreet Singh Arora[a,*]

[a] Department of Mechanical Engineering, School of Engineering, Shiv Nadar University, Uttar Pradesh 201314, India
[b] Department of Materials Science and Engineering, University of North Texas, Denton, TX 76203, USA
[c] Center for Nanoscale Materials, Argonne National Laboratory, Argonne, IL 60439, USA

ARTICLE INFO

*Keywords:*
Metallic glasses
Structural relaxation
Thermo-mechanical processing,
hydrophobicity, corrosion behavior

ABSTRACT

Amorphous metals, also known as bulk metallic glasses, are promising materials for advanced healthcare applications. This is attributed to their exceptional properties, unseen in crystalline materials. Their unique ability to undergo relaxation during low temperature annealing provides opportunity to develop tailored properties. Here, we show a new pathway to significantly accelerate the relaxation kinetics in a zirconium based metallic glass through severe surface deformation using thermo-mechanical processing. The combined strain and thermal field during thermo-mechanical processing significantly reduced the relaxation time compared to vacuum annealing concurrent with remarkable enhancement in its bio-corrosion resistance. The corrosion resistance was found to have a direct correlation with the wetting behavior and oxide layer composition. The surface of relaxed glass was found to be rich in zirconium oxide compared to its as-cast state with higher fraction of aluminum oxide. The difference in oxide layer composition was attributed to annihilation of free volume in relaxed glass resulting in limited atomic transport. Relaxed metallic glass exhibited more hydrophobic nature likely due to its lower surface energy state as a consequence of structural densification. In addition, the relaxed glass showed better cell proliferation, thereby, enhancing its appeal as a next-generation biomaterial.

## 1. Introduction

Degradation of bio-implants in the physio-chemical environment of the human body necessitates development of advanced materials with superior surface properties. Metallic glasses are a relatively new class of biomaterials with attractive surface properties [1] and unique thermoplastic processing ability for achieving intricate geometries [2–4]. Amorphous alloys show homogeneous microstructure down to the atomic scale due to absence of grains and grain boundaries. Their exceptional mechanical properties, superior corrosion and wear resistance, and biocompatibility for certain compositions make them attractive for bio-implant applications [5,6]. Metallic glasses have high elastic limit of nearly 2% which is comparable to bone's elastic limit of ~1% [7]. This provides metallic glasses a unique ability to flex elastically in synchronization with the human bone, ensuring uniform stress distribution along with reduced stress shielding effect [7]. The use of metallic glasses for bio-implant applications is further favored by their near bone compatible elastic modulus of 25–150 GPa [7] compared to ~200 GPa for commercially used stainless steel and ~110 GPa for titanium-based biomaterials [8]. Additionally, the unique thermoplastic forming ability in metallic glasses provides opportunity to develop hierarchical surface structures with adaptable functionalities [9–12].

The bulk mechanical and surface properties of a metallic glass may be tuned over a wide range by controlling it's quenched in free-volume. Rejuvenation [13] and structural relaxation by thermal strain have been shown to significantly influence the toughness [14], hardness [15,16], density [17] and elastic modulus [17,18] of metallic glasses. In all these studies, free volume changes were achieved through temperature modulation. However, there are few reports and very limited understanding on the combined influence of strain field and temperature on the corrosion behavior of metallic glasses, particularly in biological media. Enhancing the properties of metallic glasses by surface modification techniques will significantly improve their appeal as a next generation biomaterial. In this study, we utilized thermo-mechanical processing to tailor the surface state of a zirconium-based metallic glass and evaluated its corrosion behavior in simulated body fluid. The relaxed glass showed significantly higher corrosion resistance

* Corresponding author.
*E-mail addresses:* Sundeep.Mukherjee@unt.edu (S. Mukherjee), harpreet.arora@snu.edu.in (H.S. Arora).

https://doi.org/10.1016/j.apsusc.2019.05.158
Received 25 February 2019; Received in revised form 20 April 2019; Accepted 14 May 2019
Available online 15 May 2019
0169-4332/ 

compared to its as-cast state, which was attributed to enhanced hydrophobicity and more stable passive layer as a consequence of free-volume annihilation.

## 2. Experimental details

A zirconium-based metallic glass with nominal composition of $Zr_{65.7}Cu_{15.6}Ni_{11.7}Al_{3.7}Ti_{3.3}$ (wt%) was chosen for evaluating the bio-corrosion response after surface modification. This alloy is one of the best glass formers with a wide super cooled liquid region. Friction stir processing was performed using a pin-less tungsten-carbide tool with 12 mm shoulder diameter. The processing was done at a fixed rotational speed of 388 rpm and transverse speed of 20 mm/min under different cooling conditions: - (a) ambient cooling, wherein the workpiece was cooled under ambient conditions (refereed as “ambient” hereafter) and (b) external cooling, wherein the workpiece was completely submerged in a pool of low-temperature liquid maintained at 273 K using external chiller unit (refereed as “cooling” hereafter). As discussed in detail later, processing under ambient conditions led to annihilation of free volume while excess free volume was created for the processing route using external cooling. This is schematically shown in the atomic-scale models in Fig. 1. A data acquisition system (National Instruments, Model no: cDAQ-9178) was used to capture the thermal history during processing. For comparison, a sample was annealed at 653 K, which is lower than the glass transition temperature of 683 K, for 24 h in a vacuum furnace (refereed as “annealed” hereafter). The amorphous nature of all specimens was determined using X-ray diffraction. The thin oxide film formed on all samples was characterized by X-ray photoelectron spectroscopy (XPS). XPS spectra of Zr, Cu, Ni, Al, Ti and O were recorded on the surface of all the samples using monochromatic Al-Kα X-ray source (1.486 keV, Scienta Omicron Nanotechnology). Differential scanning calorimeter (DSC, Netzsch DSC 404 F1 Pegasus calorimeter), where samples were heated at 20 K/min, was used to determine the glass-transition temperature ($T_g$), crystallization temperature ($T_x$) and enthalpy changes ($\Delta H$). Surface roughness for all samples was determined using high resolution 3D optical profilometer. Static contact angle measurements were done using a goniometer (Apex instruments, ACAM-D1) by sessile drop technique. MDCK cell line was used to study the cell viability using colorimetric MTT (3-(4,5-dimethylthiazol-2-yl)-2,5-diphenyltetrazolium bromide) assay and cell morphology were captured using Actin and DAPI staining under fluorescence microscopy, the specific details of which are given elsewhere [19]. Corrosion behavior of as-cast, processed and annealed samples was evaluated using Gamry Interface 1000E electrochemical setup. A standard three electrode cell configuration was used with saturated calomel electrode (*SCE*) as reference, high density graphite rod as counter, and sample as working electrode. Ringer solution, a simulated body fluid, was used as the electrolyte. Potentiodynamic polarization was done in the voltage range of $-0.25$ V vs $E_{OCP}$ to $+0.4$ V vs $E_{OCP}$ at 0.166 mV/s scan rate. Electrochemical Impedance Spectroscopy (EIS) measurements were obtained at $E_{OCP}$ over a frequency range of 0.01 Hz to 100 kHz with a set AC voltage amplitude of 10 mV. Scanning electron microscope (SEM) (FEI environmental scanning electron microscope with built-in EDS facility) was used to study the morphology of the corroded specimens.

## 3. Results and discussion

### 3.1. Microstructure and structural relaxation

X-ray analysis of as-cast, processed and annealed metallic glass specimen is shown in Fig. 2(a). All samples showed the characteristic broad peak which confirms a fully amorphous structure. DSC thermograms for all specimens are shown in Fig. 2(b) while Fig. 2(c) shows the zoomed-in region close to the glass transition. The quantitative results of DSC are summarized in Table 1. The small exothermic peak prior to $T_g$ is an indication of structural relaxation and quantifies free volume in metallic glasses [20,21]. It is seen that enthalpy of structural relaxation ($\Delta H$) is maximum for the cooling specimen, followed by as-cast BMG, annealed and least for ambient specimen. Thus, processing under

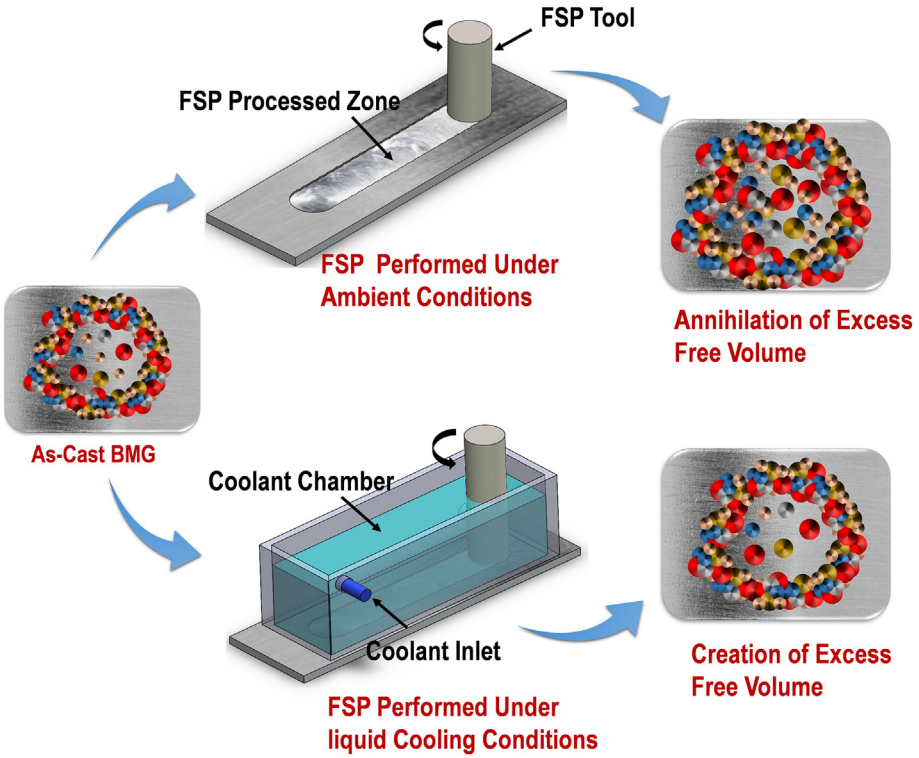


**Fig. 1.** Schematic of friction stir processing of $Zr_{65.7}Cu_{15.6}Ni_{11.7}Al_{3.7}Ti_{3.3}$ bulk metallic glass under two different conditions. Processing under ambient cooling resulted in free volume annihilation while processing under low temperature liquid enhanced the free volume of the metallic glass.

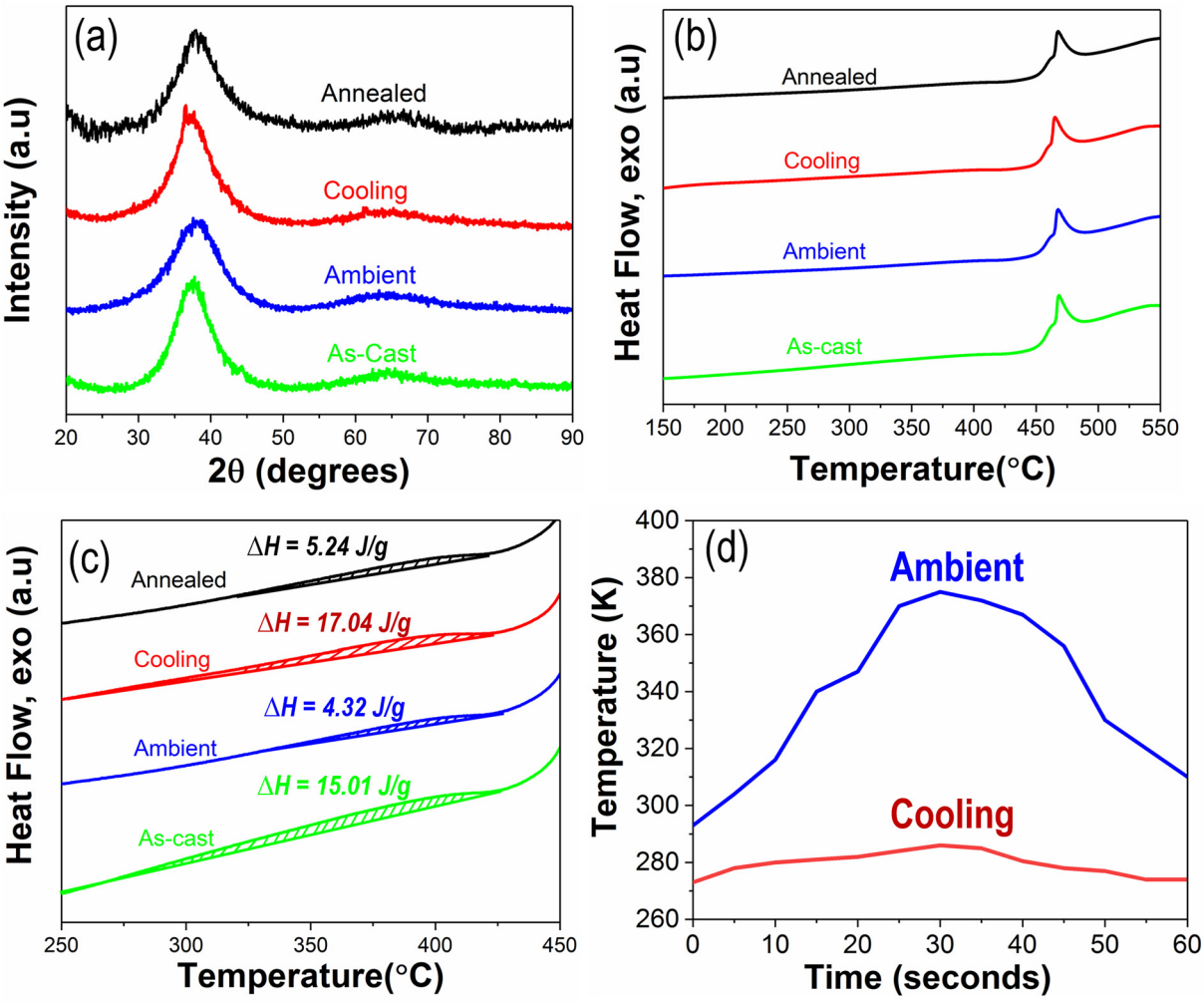


**Fig. 2.** (a) X-ray diffraction (XRD) analysis of the as-cast, ambient, cooling and annealed metallic glass specimens; (b) Differential scanning calorimetry (DSC) analysis for all samples, (c) zoom-in image of the region marked in (b), (d) temperature-time plots for ambient and cooling samples.

**Table 1**
Glass transition temperature ($T_g$), crystallization temperature ($T_x$) and enthalpy of structural relaxation ($\Delta H$) for all specimens.

| Samples | $T_g$ (°C) | $T_x$ (°C) | ΔH (J/g) |
|---|---|---|---|
| As-cast | 417 ± 2.5 | 441 ± 2.7 | 15.01 ± 0.91 |
| Ambient | 419 ± 2.2 | 448 ± 2.0 | 4.32 ± 0.17 |
| Cooling | 420 ± 3.1 | 443 ± 2.9 | 17.04 ± 0.83 |
| Annealed | 418 ± 3.2 | 446 ± 2.4 | 5.24 ± 0.13 |

ambient conditions led to significant reduction in free volume while deformation under external cooling has the contrary effect. Typically, plastic deformation increases the free volume in a metallic glass [15,22] while sub-$T_g$ annealing results in its annihilation due to structural relaxation [14,21]. In the current study, processing was done at constant tool rotational and transverse speeds, so both the samples were subjected to nearly similar strain fields. However, the thermal history was different. The temperature-time profiles for both processed conditions are shown in Fig. 2(d). The peak temperature reached for cooling and ambient samples was estimated to be nearly 280 K and 380 K, respectively. Temperature rise for cooling specimen was negligible and therefore, increase in its free volume may be attributed largely to plastic deformation. In contrast, processing under ambient conditions exposed the metallic glass to an elevated temperature field for the duration of nearly a minute (Fig. 2(d)). The short transient temperature field likely resulted in substantial drop in free volume for ambient specimen. It can be seen that the free volume difference between annealed sample and ambient specimen is marginal, indicating that 24 h of furnace annealing at 653 K likely led to similar atomic-scale rearrangement as a minute of high strain deformation. The study performed by Jian et al. [23] on the same metallic glass composition showed ~60% reduction in relaxation enthalpy after 30 min annealing at 583 K while it is nearly 80% for the 24 h annealed sample at 653 K in the current study. In contrast, the ambient processed sample showed nearly 80% reduction after 1 min exposure to combined deformation and low temperature thermal field. This indicates that the combined influence of strain energy and temperature field significantly accelerate the relaxation kinetics though atomic-scale readjustments. There was no appreciable change in the glass-transition and crystallization temperatures after processing (Table 1).

### 3.2. Electro-chemical behavior

Fig. 3(a) shows the open circuit potential for all the cases. The ambient specimen showed highest potential which indicates its nobler behavior, followed by annealed, as-cast and the least for the cooling specimen. The results of potentiodynamic polarization for all specimen are shown in Fig. 3(b). The corrosion current density ($i_{corr}$) for all specimen was determined using Tafel fitting and the corrosion penetration rate was calculated using Faraday's law (Table 2). It can be seen that $i_{corr}$ and CPR are the least for ambient specimen followed by annealed and as-cast specimens and highest for cooling specimen. The

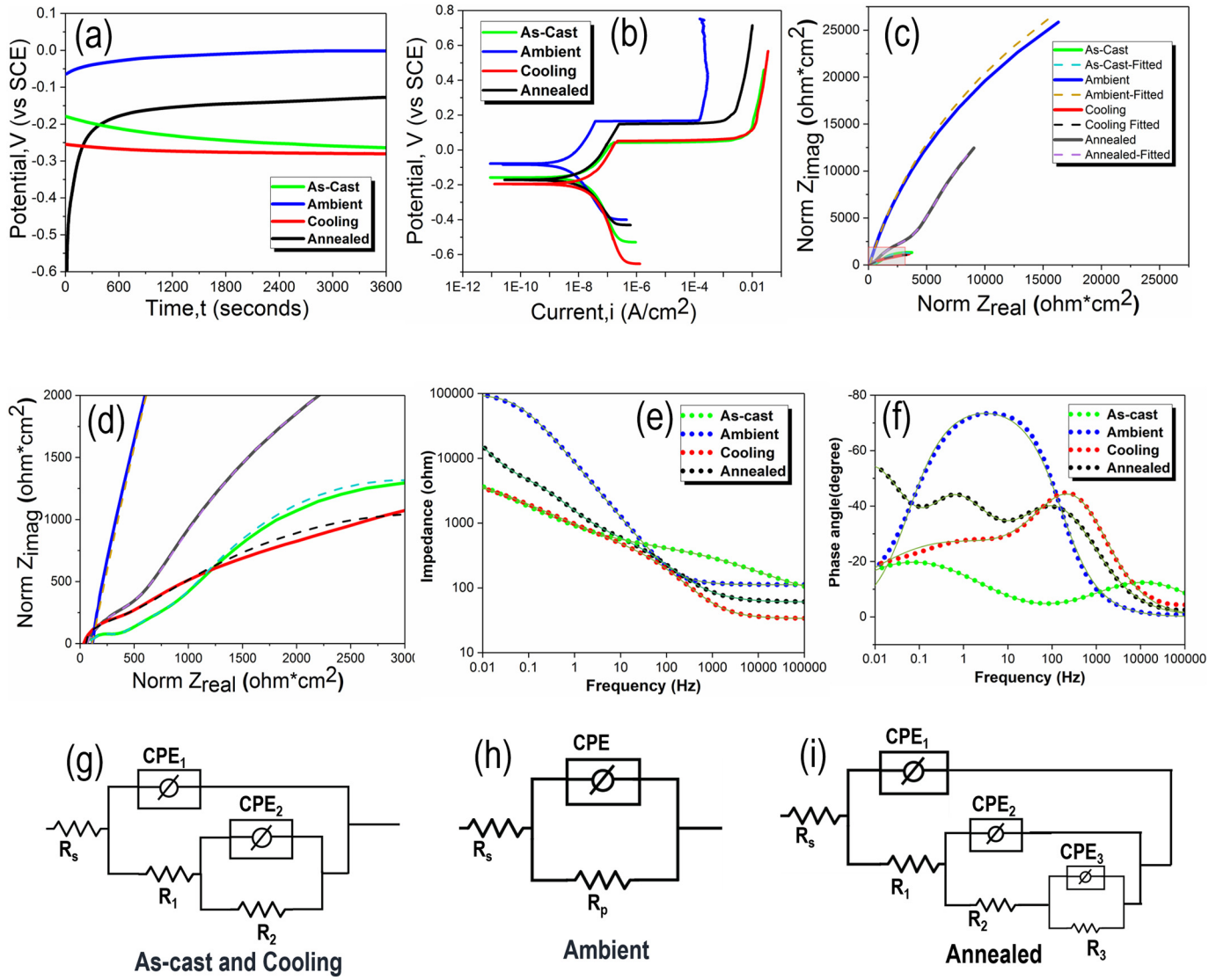


**Fig. 3.** (a) Open circuit potential as a function of time, (b) potentiodynamic polarization curves, (c) Nyquist plot for the as-cast, ambient, cooling and annealed metallic glass specimens in simulated body fluid (Ringer's solution) obtained from electrochemical impedance spectroscopy (EIS), (d) shows the zoom-in region of the area marked in (c), Bode plot showing (e) impedance vs frequency and (f) phase angle vs frequency; Equivalent electrical circuit (EEC) for (g) as-cast and cooling samples, (h) ambient sample and (i) annealed sample.

corrosion rates for ambient and annealed samples were similar and significantly smaller compared to the as-cast metallic glass. In contrast, cooling specimen showed inferior corrosion performance, worst amongst all cases. The rapid surge in corrosion current at the pitting potential is followed by quick passivation, indicated by steep rise in potential at nearly constant current density. Clearly, ambient specimen showed better passivation compared to all other specimen which further substantiate its superior corrosion resistance. Nyquist plot obtained from electrochemical impedance spectroscopy (EIS) for all cases are shown in Fig. 3(c) while Fig. 3(d) shows the zoomed-in image of the region marked in Fig. 3(c). The impedance spectrum is the highest for ambient specimen indicating its highest polarization resistance and least for cooling, in line with the results of potentiodynamic polarization. Here also, annealed showed nearly similar results as that of ambient specimen. Therefore, corrosion response was proportional to the amount of free volume i.e. - smaller the free volume of a sample, higher the corrosion resistance. Fig. 3(e) and (f) shows the Bode plot for all the specimens. The plot shows three time constants for the annealed sample whereas two time constants for the as-cast and cooling specimen, while a single time constant for the ambient sample indicating different

**Table 2**
Open circuit potential (*OCP*), corrosion potential ($E_{corr}$), corrosion current density ($I_{corr}$), corrosion per year (*mpy*), pitting potential ($E_{pit}$) and polarization resistance ($R_p$) for all specimen.

| Samples | OCP (mV) | $E_{corr}$ (mV) | $I_{corr}$ (nA/cm$^2$) | CPY (mpy) | Epit (mV) | Rp (k ohm cm$^2$) |
|---|---|---|---|---|---|---|
| As-cast | −264 ± 13 | −159 ± 11 | 29.30 ± 1.41 | 0.015 ± 0.0007 | 53 ± 12 | 5.9 ± 0.75 |
| Ambient | −7 ± 10 | −81 ± 8 | 8.63 ± 0.29 | 0.004 ± 0.0002 | 167 ± 7 | 107 ± 3.3 |
| Cooling | −281 ± 12 | −194 ± 9 | 30.40 ± 1.33 | 0.015 ± 0.0006 | 46 ± 8 | 6.07 ± 0.65 |
| Annealed | −127 ± 11 | −178 ± 16 | 12.07 ± 0.82 | 0.006 ± 0.0003 | 146 ± 11 | 80 ± 4.4 |

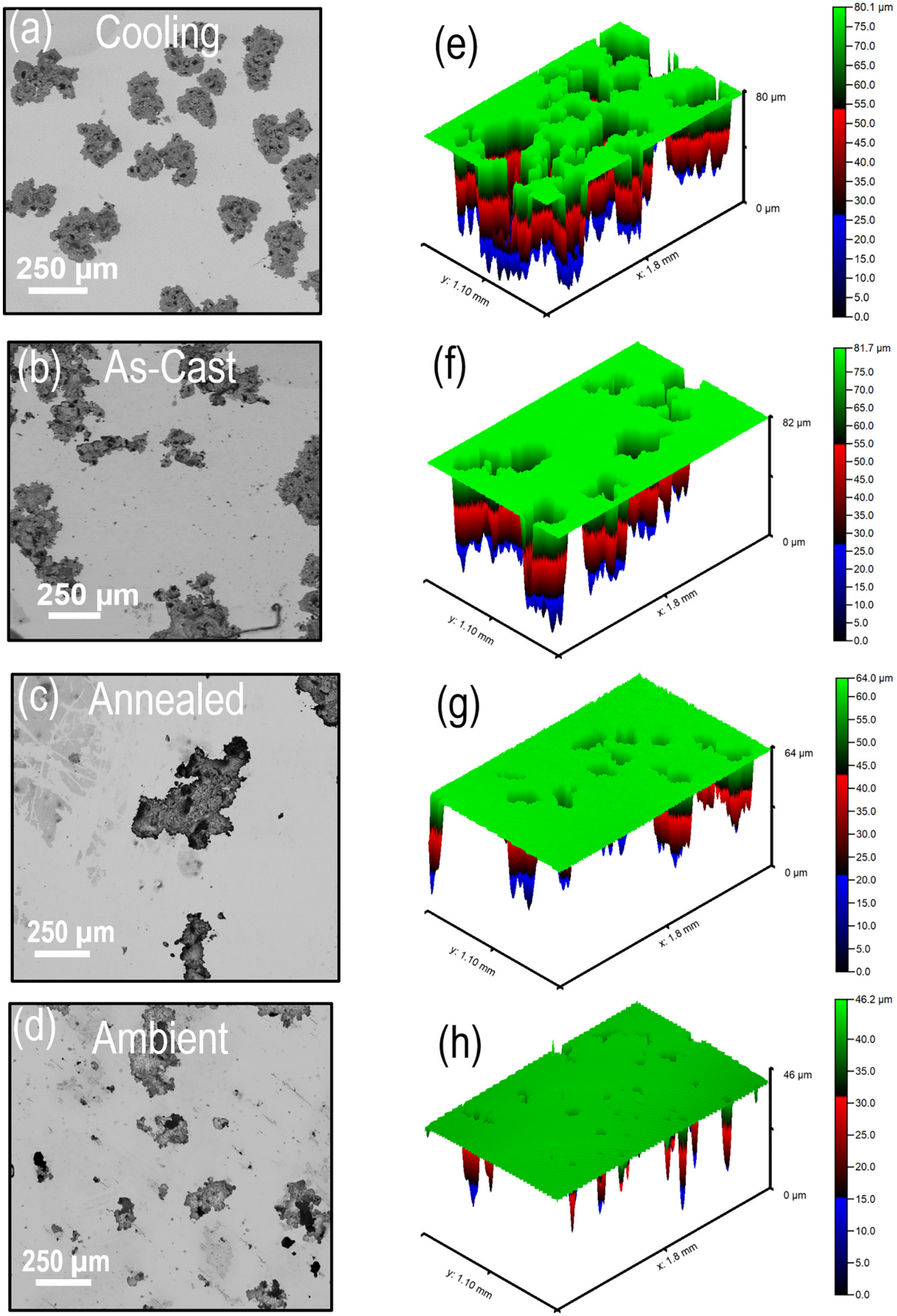


**Fig. 4.** Scanning electron microscopy (SEM) images after corrosion testing for (a) cooling, (b) as-cast, (c) annealed, (d) ambient; 3D optical profilometer images showing corrosion pit morphology for (e) cooling, (f) as-cast, (g) annealed and (h) ambient.

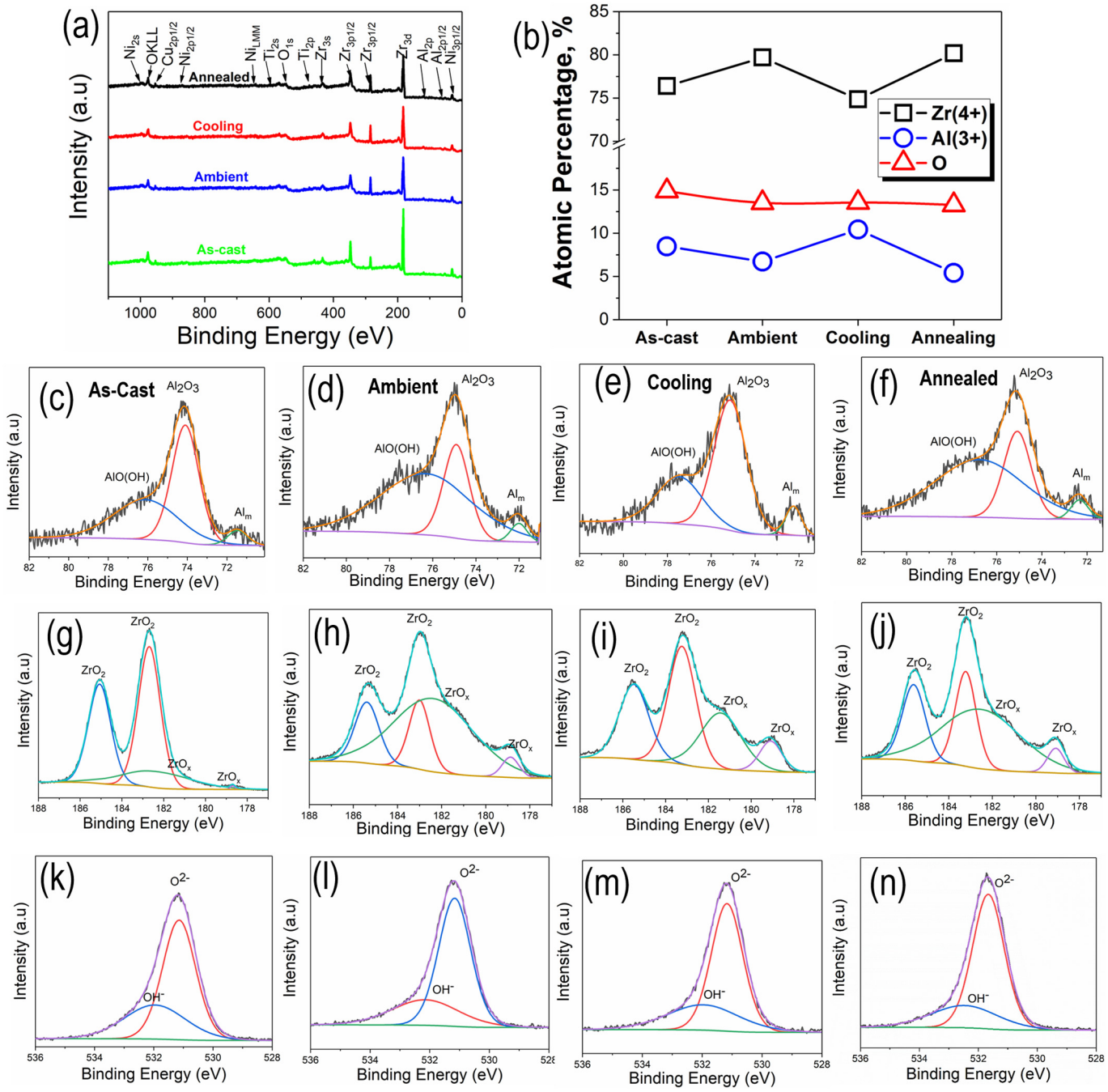


**Fig. 5.** (a) X-ray photoelectron spectroscopy (XPS) wide scan for the as-cast, ambient, cooling and annealed metallic glass specimens, (b) Quantification of the composition of oxide layer, High resolution XPS scans of (c) to (f) Al-2P, (g) to (j) Zr-3d and (k) to (n) O-1s for all specimen.

behavior of the passive layer. At higher frequencies, the phase angle in all cases drops nearly to 0°, representing the electrolyte resistance [24]. At middle frequencies, the phase angle remain close to −70° for the ambient sample indicating near capacitive response, while it varies for other samples due to multiple time constants. The electrical equivalent circuit (EEC) used to fit the obtained EIS data are shown in Fig. 3(g) through (i). The fitted curve agreed well with the obtained data.

Scanning electron microscopy (SEM) images of the corroded surfaces for all cases are shown in Fig. 4(a) to (d). Both as-cast and cooling specimen showed extensive corrosion in the form of high density of wide corrosion pits. In contrast, the surface of ambient and annealed specimens showed lower pit density supporting its superior corrosion resistance. The 3D optical profilometer images of corrosion pits for all samples are shown in Fig. 4(e) to (h). The pit depth for as-cast and cooling samples was found to be nearly 70–75 μm compared to nearly 55 μm for the annealed and 35 μm for the ambient specimen, supporting highest corrosion resistance of the ambient specimen. Corrosion behavior is known to be dependent on number of factors, especially surface composition, roughness and wettability characteristics. Surface composition in each case was determined using XPS and the results are shown in Fig. 5. XPS wide scan (Fig. 5(a)) are similar for all samples indicating nearly similar composition of the passive layer. Fig. 5(b) gives the quantification of Zr (4+) and Al (3+) and (O) for all samples, indicating higher Zr fraction for both annealed and ambient samples while as-cast and cooling samples are relatively rich in Al. The XPS scans for Al-2P, Zr-3d, and O-1s for all samples are shown in Fig. 5(c) to (n) indicating $Al_2O_3$ and $ZrO_2$ as the primary constituents of the passive layer in all the cases. The standard electrode potential of $Zr/Zr^{4+}$

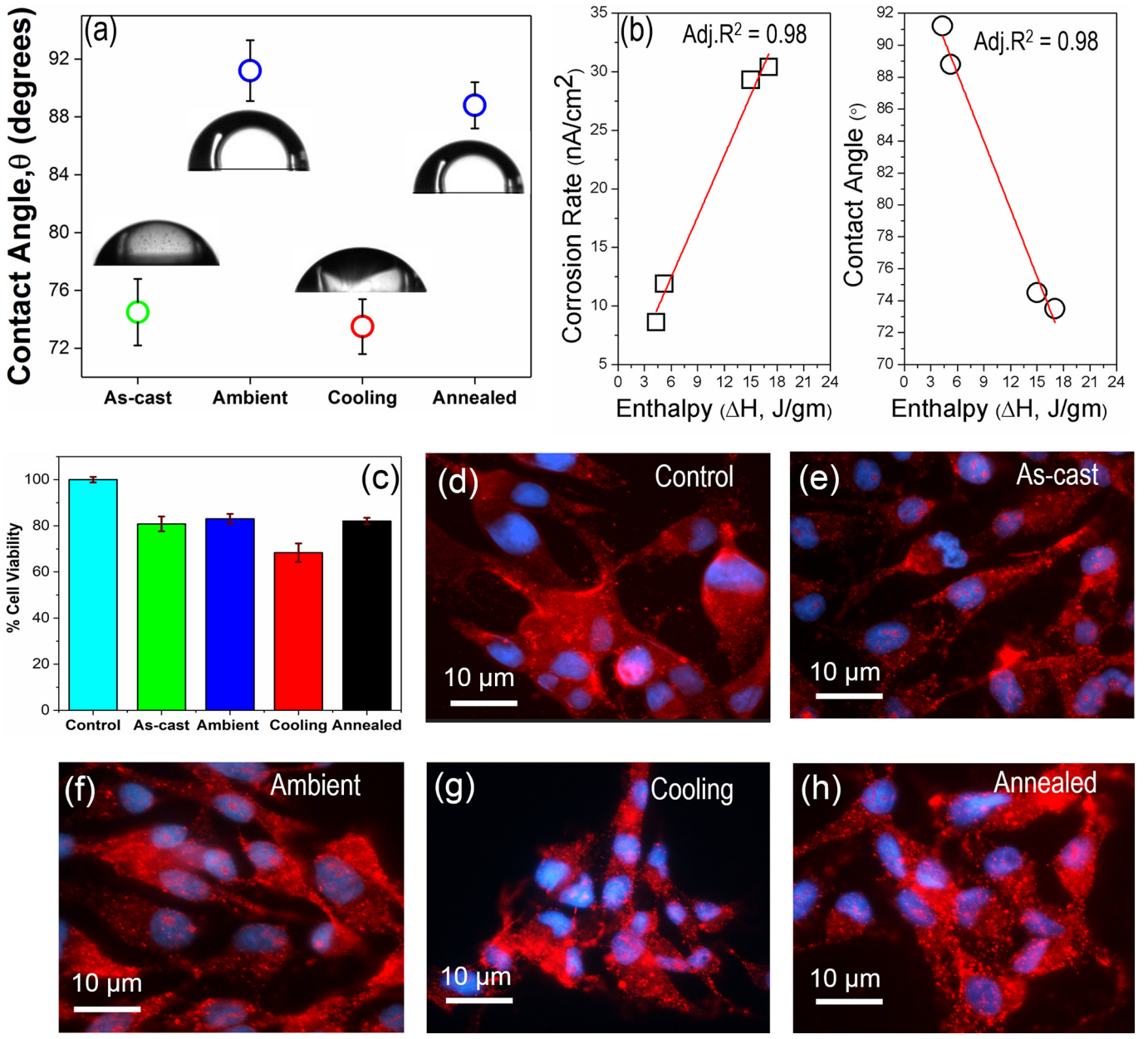


**Fig. 6.** (a) Contact angle for the as-cast, ambient, cooling and annealed metallic glass specimens, (b) variation of corrosion rate and contact angle as a function of relaxation enthalpy, (c) Tryphan blue exclusion assay, percentage of living MDCK cells; fluorescence micrographs of MDCK cells (d) Polystyrene (Control), (e) as-cast, (f) ambient, (g) cooling and (h) annealed metallic glass specimens.

(1.45 V) and $Al/Al^{3+}$ (1.677 V) are higher compared to rest of the composition which likely leads to rapid formation of $ZrO_2$ and $Al_2O_3$ [25,26]. Further, higher Zr fraction in ambient and annealed specimen indicates that the oxide layer formed on these specimens were rich in $ZrO_2$ while cooling and as-cast specimen was rich in $Al_2O_3$. The difference in oxide layer composition can be explained in terms of atomic transport in metallic glasses. The long-range atomic transport in supercooled liquid occurs by single-atom hopping [27]. Typically, the activation energy for diffusion in a relaxed glass is higher compared to its as-cast state [27,28] which reduces the atomic transport in a relaxed glass. Thus, with least free volume, the atomic diffusivity is likely to be lower for annealed and ambient specimens, lowering the Al content in the oxide layer, the element with the smallest atomic radius in the investigated glass. Lower corrosion rate for ambient and annealed specimen also correlates well with the higher fraction of $ZrO_2$ which is known to have excellent corrosion resistance [29]. The average roughness ($R_a$) and root mean square roughness ($R_{rms}$), obtained using optical profiler, was found to be similar for all specimen and thus unlikely to have any influence on the corrosion behavior.

### 3.3. Wettability and cell-proliferation

The wettability for all samples, probed using contact angle measurements, is shown in Fig. 6(a). Ambient and annealed specimens showed highest static contact angle of nearly 91° and 89° followed by as-cast and least for cooling specimen with nearly 73° contact angle. Thus, ambient and annealed specimen showed more hydrophobic nature compared to cooling and the as-cast glass. The nature of oxide layer and sub-surface interactions can play an important role in determining the wettability. The water contact angle for $ZrO_2$ and $Al_2O_3$, the two major constituents of oxide layer, is nearly similar, i.e. 71.8° and 72.4° respectively [30]. Thus, the difference in wettability across

difference specimens can be due to sub-surface interactions rather than the oxide layer. Typically, the thickness of pristine oxide layer on most materials is of the order of few nanometers. At these length-scales, the long range van der Waals forces are effective and the sub-surface free energy can have substantial influence on the interacting species [31]. With larger structural relaxation, the free energy for both ambient and annealed samples is likely to be lower, making them more hydrophobic compared to other two specimens. Further, the van der Waal interactions, which are proportional to the dispersion component of surface free energy, are likely to be stronger for as-cast and cooling specimen, resulting in lower contact angle. Therefore, the observed difference in wettability can be attributed to changes in free volume content, leading to different surface energy states in the glass. The dependence of contact angle on relaxation enthalpy is shown in Fig. 6(b) which signifies a direct correlation between the two. Also, the corrosion rate for all specimen varies linearly with the relaxation enthalpy (Fig. 6(b)). Thus, wettability, corrosion behavior and free volume content are strongly correlated in a metallic glass with the later acting as a primary governing factor. Therefore, superior corrosion resistance of ambient and annealed specimen may be attributed to combined influence of increased hydrophobicity and higher zirconium fraction in the oxide layer, both of which are the consequence of free volume annihilation through relaxation. All the samples were found to be compatible to MDCK cell line with minor difference in the cell viability (Fig. 6(c)). The cell proliferation on annealed and ambient samples was seen to be similar to the control with elongated morphology, while cells tend to segregate and acquire an unfavorable round morphology on the cooling specimen (Fig. 6(d) to (h)). This is likely attributed to higher fraction of $ZrO_2$ in the passive layer of ambient and annealed specimens which is known to have excellent biocompatibility. Thus, the current study suggests that deformation-assisted low temperature annealing could provide a novel pathway for developing multifunctional bio-implant materials with superior corrosion-resistance, higher reliability and favorable bio-adaptable traits.

## 4. Conclusions

In summary, severe deformation under ambient conditions was found to significantly accelerate relaxation kinetics in a zirconium-based bulk metallic glass. The atomic-scale rearrangement during severe deformation for nearly a minute was found to be nearly similar to 24 h of furnace annealing at 653 K. In contrast, deformation accompanied by rapid cooling resulted in free volume increase. The relaxed glass showed significantly lower corrosion rate compared to as-cast glass in simulated body fluid. The corrosion rate and contact angle for different metallic glass samples showed a strong correlation with the free volume content. Higher corrosion resistance of relaxed glass is explained by increased hydrophobicity and higher fraction of zirconium oxide in the passive layer. In addition, the relaxed glass also showed better cell-proliferation with favorable cellular morphology.

## Acknowledgements

This research was supported by the project titled "*Tailoring the Surface Properties of Crystalline and Amorphous Metals for Advanced Bio-Implants*" (File no. YSS/2015/000678) by the Science and Engineering Research Board (SERB), Department of Science and Technology (DST), India. S.M. acknowledges funding from the National Science Foundation (NSF) under Grant Number 1762545 (CMMI). Any opinions, findings, and conclusions expressed in this paper are those of the authors and do not necessarily reflect the views of the National Science Foundation (NSF).

## References

[1] S. Katakam, H. Singh Arora, S. Mukherjee, N.B. Dahotre, Amorphous coatings and surfaces on structural materials AU - Joshi, Sameehan S, critical reviews in solid state and materials, Sciences 41 (2016) 1–46.
[2] G. Kumar, H.X. Tang, J. Schroers, Nanomoulding with amorphous metals, Nature 457 (2009) 868.
[3] G. Kumar, P.A. Staffier, J. Blawzdziewicz, U.D. Schwarz, J. Schroers, Atomically smooth surfaces through thermoplastic forming of metallic glass, Appl. Phys. Lett. 97 (2010) 101907.
[4] G. Duan, A. Wiest, M.L. Lind, J. Li, W.-K. Rhim, W.L. Johnson, Bulk metallic glass with benchmark thermoplastic processability, Adv. Mater. 19 (2007) 4272–4275.
[5] J. Schroers, G. Kumar, T.M. Hodges, S. Chan, T.R. Kyriakides, Bulk metallic glasses for biomedical applications, JOM 61 (2009) 21–29.
[6] Y. Liu, J. Padmanabhan, B. Cheung, J. Liu, Z. Chen, B.E. Scanley, D. Wesolowski, M. Pressley, C.C. Broadbridge, S. Altman, U.D. Schwarz, T.R. Kyriakides, J. Schroers, Combinatorial development of antibacterial Zr-Cu-Al-Ag thin film metallic glasses, Sci. Rep. 6 (2016) 26950.
[7] H.F. Li, Y.F. Zheng, Recent advances in bulk metallic glasses for biomedical applications, Acta Biomater. 36 (2016) 1–20.
[8] M. Niinomi, Mechanical properties of biomedical titanium alloys, Mater. Sci. Eng. A 243 (1998) 231–236.
[9] S. Mukherjee, R.C. Sekol, M. Carmo, E.I. Altman, A.D. Taylor, J. Schroers, Tunable hierarchical metallic-glass nanostructures, Adv. Funct. Mater. 23 (2013) 2708–2713.
[10] H.S. Arora, Q. Xu, Z. Xia, Y.-H. Ho, N.B. Dahotre, J. Schroers, S. Mukherjee, Wettability of nanotextured metallic glass surfaces, Scr. Mater. 69 (2013) 732–735.
[11] M. Hasan, J. Schroers, G. Kumar, Functionalization of metallic glasses through hierarchical patterning, Nano Lett. 15 (2015) 963–968.
[12] E.R. Kinser, J. Padmanabhan, R. Yu, S.L. Corona, J. Li, S. Vaddiraju, A. Legassey, A. Loye, J. Balestrini, D.A. Solly, J. Schroers, A.D. Taylor, F. Papadimitrakopoulos, R.I. Herzog, T.R. Kyriakides, Nanopatterned bulk metallic glass biosensors, ACS Sensors 2 (2017) 1779–1787.
[13] S.V. Ketov, Y.H. Sun, S. Nachum, Z. Lu, A. Checchi, A.R. Beraldin, H.Y. Bai, W.H. Wang, D.V. Louzguine-Luzgin, M.A. Carpenter, A.L. Greer, Rejuvenation of metallic glasses by non-affine thermal strain, Nature 524 (2015) 200.
[14] U. Ramamurty, M.L. Lee, J. Basu, Y. Li, Embrittlement of a bulk metallic glass due to low-temperature annealing, Scr. Mater. 47 (2002) 107–111.
[15] S. Xie, E.P. George, Hardness and shear band evolution in bulk metallic glasses after plastic deformation and annealing, Acta Mater. 56 (2008) 5202–5213.
[16] J. Gu, M. Song, S. Ni, S. Guo, Y. He, Effects of annealing on the hardness and elastic modulus of a Cu36Zr48Al8Ag8 bulk metallic glass, Mater. Des. 47 (2013) 706–710.
[17] H.S. Chen, The influence of structural relaxation on the density and Young's modulus of metallic glasses, J. Appl. Phys. 49 (1978) 3289–3291.
[18] H.S. Arora, A.V. Aditya, S. Mukherjee, Structural relaxation driven increase in elastic modulus for a bulk metallic glass, J. Appl. Phys. 117 (2015) 014902.
[19] G. Perumal, A. Ayyagari, A. Chakrabarti, D. Kannan, S. Pati, H.S. Grewal, S. Mukherjee, S. Singh, H.S. Arora, Friction stir processing of stainless steel for ascertaining its superlative performance in bioimplant applications, ACS Appl. Mater. Interfaces 9 (2017) 36615–36631.
[20] A. van den Beukel, J. Sietsma, The glass transition as a free volume related kinetic phenomenon, Acta Metall. Mater. 38 (1990) 383–389.
[21] Y. Xu, J. Fang, H. Gleiter, H. Hahn, J. Li, Quantitative determination of free volume in Pd40Ni40P20 bulk metallic glass, Scr. Mater. 62 (2010) 674–677.
[22] R. Bhowmick, R. Raghavan, K. Chattopadhyay, U. Ramamurty, Plastic flow softening in a bulk metallic glass, Acta Mater. 54 (2006) 4221–4228.
[23] W.H. Jiang, F. Jiang, B.A. Green, F.X. Liu, P.K. Liaw, H. Choo, K.Q. Qiu, Electrochemical corrosion behavior of a Zr-based bulk-metallic glass, Appl. Phys. Lett. 91 (2007) 041904.
[24] Y.B. Wang, H.F. Li, Y. Cheng, S.C. Wei, Y.F. Zheng, Corrosion performances of a nickel-free Fe-based bulk metallic glass in simulated body fluids, Electrochem. Commun. 11 (2009) 2187–2190.
[25] J. Qiao, J. Fan, F. Yang, X. Shi, H. Yang, A. Lan, The corrosion behavior of Ti-based metallic glass matrix composites in the H2SO4 solution, Metals 8 (2018) 52.
[26] H.F. Tian, J.W. Qiao, H.J. Yang, Y.S. Wang, P.K. Liaw, A.D. Lan, The corrosion behavior of in-situ Zr-based metallic glass matrix composites in different corrosive media, Appl. Surf. Sci. 363 (2016) 37–43.
[27] X.P. Tang, U. Geyer, R. Busch, W.L. Johnson, Y. Wu, Diffusion mechanisms in metallic supercooled liquids and glasses, Nature 402 (1999) 160.
[28] T. Zumkley, V. Naundorf, M.-P. Macht, G. Frohberg, Effect of reversible structural relaxation on diffusion in bulk metallic glasses, Ann. Chim. Sci. Mater. 27 (2002) 55–60.
[29] E. McCafferty, Introduction to Corrosion Science, Springer, New York, 2010.
[30] M.L. González-Martín, L. Labajos-Broncano, B. Jańczuk, J.M. Bruque, Wettability and surface free energy of zirconia ceramics and their constituents, J. Mater. Sci. 34 (1999) 5923–5926.
[31] J.N. Israelachvili, Intermolecular and Surface Forces, Elsevier Science, 2015.